Molecular and Nanoscale Compositional Contrast of Soft Matter in Liquid: Interplay between Elastic and Dissipative Interactions

Amir F. Payam,[†] Jorge R. Ramos, and Ricardo Garcia*

IMM-Instituto de Microelectrónica de Madrid, CSIC, Isaac Newton 8, Tres Cantos, 28760 Madrid, Spain. [†]Present address: School of Electrical & Computer Engineering, University of Tehran, Iran.

ABSTRACT

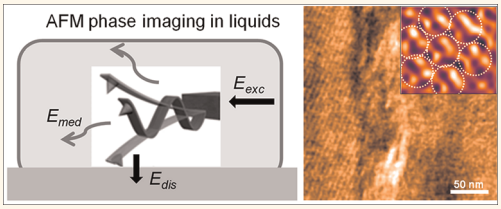

We demonstrate that the phase contrast observed with an amplitude modulation atomic force microscope depends on two factors, the generation of higher harmonics components and the energy dissipated on the sample surface. Those factors are ultimately related to the chemical composition and structure of the surface. Our findings are general, but they specifically describe the results obtained while imaging soft materials in liquid. Molecular resolution experiments performed on a protein membrane surface in liquid confirm the theory.

KEYWORDS: surface properties · amplitude modulation atomic force microscopy · mechanical properties · compositional contrast · protein membranes

In amplitude modulation atomic force microscopy (AM-AFM), the phase shift between the excitation signal and the cantilever-tip response is a powerful source of material contrast. In addition to provide information about compositional changes,[1−13] AFM phase imaging enables the quantification of energy-dissipation processes at the nanoscale.[14−24] Recently, the relevance of phase imaging has been highlighted by four applications: (1) to provide information on subsurface properties in cells[7,25] and polymers;[12,26] (2) to map interfacial energies with molecular resolution;[6,27] (3) to identify energy-dissipation processes with nanoscale spatial resolution;[21] and (4) to enhance material contrast of mechanical[28−30] and magnetic properties[31,32] in bimodal AFM. In fact, the qualitative information provided by AFM phase imaging is one of the reasons that explain the expansion of force microscopy in material sciences. However, the usefulness of phase imaging in liquid strongly depends on the understanding of the factors that control the phase-shift contrast. Thus, despite the growing interest and relevance of AFM phase imaging to enhance compositional contrast of soft materials, a comprehensive and general model is yet to be established.

The theory of AFM phase imaging for high-quality factors Q (20−1000) (air environments) is well established. It is usually expressed in terms of the relationship between the sine of the phase shift and the energy transferred (dissipated) to the sample surface.[14,15] A complementary expression in terms of the cosine of the phase shift has also been deduced.[33] The theory assumes a sinusoidal tip's response, and it has been validated by several experimental observations[14,34,35] and numerical simulations.[21,23] However, the above theory is not valid to describe experiments performed in liquid environments or, in other words, experiments using low Q cantilevers (1−10) where the tip motion contains higher harmonics components. In fact, by using a point-mass model to describe the cantilever motion, Tamayo showed that the sine of the phase shift also carries contributions from the second harmonic component of the tip's oscillation.[36] Recently, Raman and co-workers proposed a model where the phase contrast observed in liquid derives from a unique energy flow channel that opens up due to the momentary excitation of the second eigenmode.[37] The model considers the cantilever as a continuous beam.[37−40] Then, the cantilever dynamics is expressed in terms of the

* Address correspondence to ricardo.garcia@imm.cnm.csic.es.

Received for review October 4, 2011 and accepted May 4, 2012.

Published online May 11, 2012
10.1021/nn2048558

contributions from the first two cantilever eigenmodes. The theory introduces a term that reflects the propagation of energy between modes. However, there is not an observable associated with it.

Here we propose a model that explains the phase contrast observed in AFM in terms of conservative and nonconservative tip−surface interactions. We deduce an equation that relates the phase shift with the generation of higher harmonics and the energy dissipated on the sample surface. The proposed model defines the ability to extract quantitative information from AFM phase images. We also show that this model is valid for both operation in liquid or air environments. Several experiments have been carried out in liquid to test the theory. The agreement obtained between the experiments performed on a purple membrane surface and the simulations confirm the theory.

RESULTS AND DISCUSSION

First, we start with the equation that describes the energy balance of the cantilever and the sample interface. In the steady-state solution, the external mechanical energy (W_{ext}) supplied by the driving force F_0 to the cantilever must be equal to the sum of the energy released to the medium by hydrodynamic damping (W_{med}) and the energy transferred to the sample surface by the tip−surface forces F_{ts} (E_{dis}). Because the cantilever has several flexural eigenmodes, the cantilever total energy is distributed among them (Figure 1a),

$$W_{ext} = W_{med} + E_{dis} = \sum_{j=1}^{M} W_{med}(j) - \int F_{ts}\dot{q}(t)\,dt \quad (1)$$

with

$$W_{ext} = \int_0^T F_0 \cos(\omega t)\dot{q}\,dt \quad (2)$$

and

$$W_{med} = \sum_{j=1}^{M} \frac{k_j}{Q_j\omega_j}\int_0^T \left(\frac{dq_j}{dt}\right)^2 dt \quad (3)$$

The cantilever deflection $q(t)$ is the sum of the contributions from all the cantilever modes (q_j).

$$q(t) = \sum_{j=1}^{M} q_j(t) \quad (4)$$

Alternatively, the cantilever deflection could be expressed in terms of the harmonics (A_n) of the driving frequency ω=2πT,

$$q(t) = \sum_{j=1}^{M} q_j(t) = \sum_{n=1}^{N} A_n \cos(n\omega t - \phi_n) \quad (5)$$

where A_n is the amplitude of the harmonic with angular frequency $n\omega$. Similarly, the cantilever

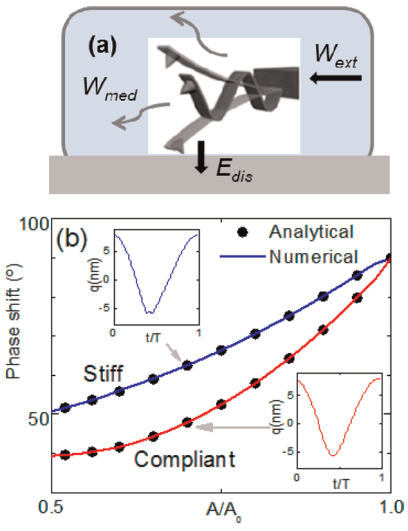

Figure 1. (a) Scheme of the energy balance for a cantilever-tip system with two eigenmodes. Three different types of energy contributions are considered, the external energy, the energy transferred to the liquid by hydrodynamic damping, and the energy transferred to the sample (dissipation). (b) Theoretical and simulated phase-shift-dependence on the amplitude for a compliant (E = 50 MPa; η = 10 Pa s) and a hard surface (E = 10 GPa). The insets show the instantaneous cantilever deflection $q(t)$ calculated for the hard (mica) and compliant (purple membrane) surfaces (A_{sp} = A/A_0 = 0.7). A clear deviation from a sinusoid waveform is observed in the bottom part of the deflection for the hard material; A_0 = 9.4 nm.

deflection associated with each eigenmode could be expressed as

$$q_j(t) \approx \sum_{n=1}^{N} A_n'(j)\cos(n\omega t - \phi_n'(j)) \quad (6)$$

where $A_n'(j)$ is the component of the nth harmonic present in the eigenmode j. To simplify the calculations and to reach an analytical expression we just consider the contributions from the first two eigenmodes (q_1, q_2). This approximation is supported by numerical simulations. Then, the deflection of second mode can be expressed in terms of the total deflection and that of the first mode as

$$q_2 = q - q_1 = \sum_{n=1}^{N} [A_n \cos(n\omega t - \phi_n) - A_n'(1)\cos(n\omega t - \phi_n'(1))] \quad (7)$$

Furthermore, it is assumed that $\phi_n'(1) \approx \phi_n'$. Then by substituting eqs 2−7 into eq 1 the following expression is deduced ($\omega = \omega_1$)

$$\sin\phi_1 = \frac{1}{\pi F_0 A_1}\left[\frac{\pi k_1}{Q_1}\sum_{n=1}^{N} n^2 A_n'^2 + \frac{\pi k_2\omega_1}{Q_2\omega_2}\sum_{n=1}^{N} n^2[A_n - A_n']^2 + E_{dis}\right] \quad (8)$$

In the above expression we have also assumed that

$$\sin \phi_n \sin \phi_n' + \cos \phi_n \cos \phi_n' \approx 1 \qquad (9)$$

Consequently, two different factors contribute to the sine of the phase shift: (1) the strength of the different higher harmonics of the excitation frequency generated by the nonlinear regions of the tip−surface force and (2) the amount of the mechanical energy of the cantilever transferred to the sample surface (dissipation). From the higher harmonics it is possible to obtain the conservative contribution of the tip−surface force.[41,42] Those contributions are present even when the feedback loop that keeps the set point amplitude at a fixed value is active (A_1 = constant). This is the main and key difference with respect to the results derived by using a point-mass model.[14,15]

A further simplification can be achieved whenever $A_n \approx A_n'$, then

$$\sin \phi_1 = \frac{1}{\pi F_0 A_1}\left[\frac{\pi k_1}{Q_1}\sum_{n=1}^{N} n^2 A_n^2 + E_{\text{dis}}\right] \qquad (10)$$

with $F_0 \approx k_1 A_0/Q_1$. We note that eq 10 coincides with the expression deduced by Tamayo.[36] The higher order components decay with the harmonic order as $1/n^2$. Furthermore, in high resolution imaging conditions in air (peak forces below 1 nN), the higher harmonic components ($n \geq 2$) are negligible with respect to A_1. Thus, from eq 8 we recover the well-known expression deduced for operation in air.[1,14,15]

The validity of eq 8 is confirmed by numerical simulations and experiments. Figure 1b shows a comparison between the analytical and the numerical simulations for a compliant and viscous material (E = 50 MPa, η=10 Pa s) and a stiff material (E = 10 GPa). In both cases, the semianalytical results match the full numerical solutions of the tip motion. A free amplitude of A_0 = 9.4 nm has been used. Similar agreement has been obtained for other values of the free amplitude and/or in the presence of dissipation. A hint about the importance of the sample stiffness on the generation of higher harmonics components is observed by comparing the bottom sections of the tip's oscillation for a stiff and a compliant material (insets in Figure 1b). The anharmonic distortion is more noticeable in the bottom part of the oscillation when the tip is interacting with the stiffer material.

In the numerical simulations, the tip−surface has been simulated by using the Derjaguin−Muller−Toporov contact model[43] and the viscous force as derived in ref 21. The behavior of different materials is described by using an effective elastic modulus and a viscosity coefficient η. At the same time, molecular resolution experiments in liquid have been performed in a high-ionic concentration buffer (see Methods) to screen long-range electrostatic interactions. These experimental conditions allow us to neglect the contribution

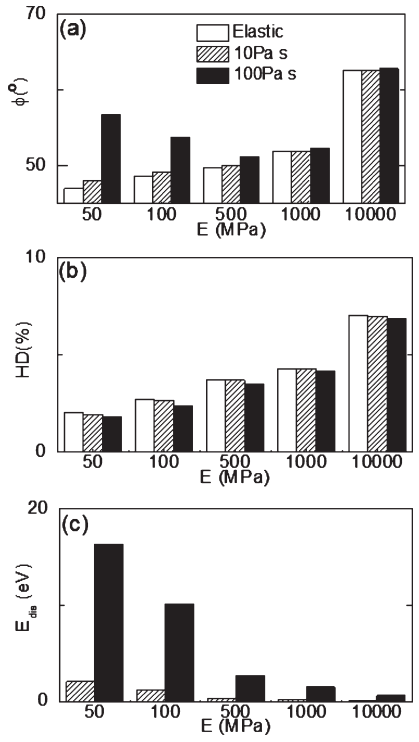

Figure 2. (a) Phase shift for materials of different elastic and viscoelastic values. (b) Harmonic distortion as a function of the elastic modulus of the sample surface for the simulations in panel a. (c) Energy dissipation for the materials and conditions simulated in panel a. Open columns means no dissipation, dashed columns are for a viscosity coefficient of 10 Pa s, and the filled columns are for a viscosity coefficient of 100 Pa s; A_{sp} = 0.7 and A_0 = 9.4 nm.

from the Derjaguin−Landau−Verwey−Overbeek forces.[37] In the simulations the parameters describing the microcantilever are k_1 = 0.22 N/m, k_2 = 12.23 N/m, f_1 = 18.6 kHz, f_2 = 170 kHz, Q_1 = 1.6, Q_2 = 4.5, R = 10 nm.

Figure 2a shows the phase-shift values obtained for different materials ($A_{sp} = A = 0.7A_0$). The plot reveals that in the absence of dissipation, the phase shift increases monotonically with the stiffness of the material (empty columns). However, a significant change of the phase-shift value is obtained in the presence of dissipation (compliant materials). The data indicate that both dissipation and higher harmonics play a significant role in the compositional contrast observed in AFM phase imaging. For example, a phase-shift difference of 5° is obtained between two materials of identical Young modulus (E = 100 MPa) but with a difference of about 10 eV in dissipation (Figure 2a,c). A similar phase-shift contrast can be obtained in the absence of dissipation between two elastic materials, one with E = 50 MPa and the other with E = 1 GPa. The former case coincides with what is observed in high Q environments (air) where the phase-shift contrast depends almost exclusively on dissipation.

Some of the above findings are illustrated in Figure 3. Figure 3a shows the phase-shift cross-section of an ideal atomically flat sample made of two elastic

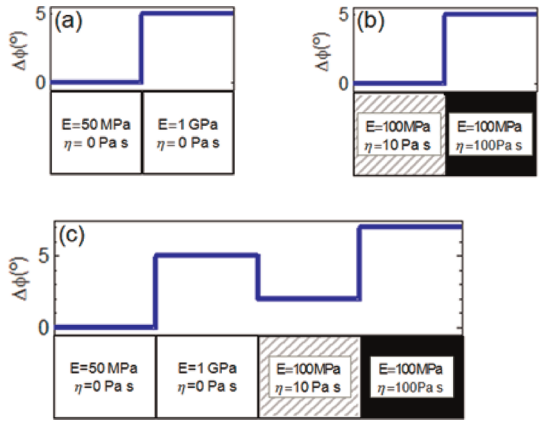

Figure 3. phase-shift cross sections for flat and heterogeneous interfaces. The plots are based on the results shown in Figure 2: (a) phase-shift cross-section for a surface made of two elastic regions; (b) phase-shift cross-section for a surface made of two inelastic regions; (c) phase shift for a surface made of the four regions described in panels a and b. In the above cases, the origin of the phase shift is the value given by the region with E = 50 MPa.

regions characterized, respectively, with a Young modulus of 50 MPa and 1 GPa. The cross-section shows a step-like jump of 5° when the tip moves from the compliant to the stiffer region. However, a similar phase-shift change could be observed on a surface made of two regions characterized by having the same effective Young modulus (100 MPa) but with different viscous coefficients, respectively, 10 and 100 Pa s (Figure 3b). A heterogeneous surface that combines the above four regions would show a phase-shift cross-section as the one plotted Figure 3c. In fact, this plot illustrates both the relative character of phase imaging measurements and their usefulness to provide spatial variations of material properties. It is worth noting that, in some cases, different materials could give the same phase-shift value.

The harmonic distortion (HD) gives more information about the role of the elastic modulus on the generation of higher harmonics components. The HD is defined as the ratio of the higher harmonics components with respect to the fundamental harmonic,

$$\mathrm{HD} = \frac{1}{A_1^2}\sum_{n=2}^{N} n^2 A_n^2 \qquad (11)$$

The harmonic distortion and, consequently, the generation of higher harmonic components increase with the elastic modulus of the sample (Figure 2b). In addition, under the same feedback conditions, that is, the same set point and free amplitudes, the phase shift also increases with the elastic modulus in the absence of dissipation. We note that for the same elastic modulus, the HD does not change significantly with the presence of realistic energy dissipation processes. On the other hand, the energy dissipated by viscoelastic processes decreases by increasing the elastic modulus of the material because the tip's indentation decreases (Figure 2c).

The minimum observed in the phase shift as a function of the elastic modulus in the presence of dissipation in Figure 2a (solid/dark columns) captures the competition between the generation of higher harmonics and the presence of energy dissipation processes. The HD increases monotonically with the elastic modulus (Figure 2b) while the energy dissipated decreases by increasing the elastic modulus (Figure 2c).

The experimental measurements could be performed at different values A or by using different free amplitudes A_0. The numerical simulations show that the phase shift decreases by decreasing the A/A_0 ratio for elastic materials (Figure 1b). In the presence of inelastic interactions the situation becomes more complicated because the phase shift might show a minimum. The harmonic distortion increases by decreasing A/A_0 for both stiff and compliant materials. On the other hand, the dissipated energy has a maximum with A/A_0 (data not shown). The latter behavior has been observed experimentally.[22]

From the above results we conclude that the phase contrast ($\Delta\phi$) observed in AFM experiments, in particular those performed in liquid environments, has two contributions, one coming from the variations of the conservative part of the nonlinear tip−surface forces and the other from the presence of dissipation processes. It happens that the nonlinear forces involved in liquid are dominated by short-range repulsive forces because the long-range attractive forces of van der Waals type are usually screened in aqueous environments. The nonlinear forces excite higher harmonics of the driving frequency (see Figure 5). The amplitude of those harmonics also contributes to the phase-shift value. In heterogeneous and elastic surfaces, the differences in the amplitude of the harmonics determine the phase contrast. In some occasions, the frequency of a given harmonic might match or be close to the frequency of an eigenmode. In those conditions, the eigenmode and the harmonics are coupled, which effectively enhances the observed amplitude of the harmonics.

The predictions of the theory have been tested experimentally. Phase-shift measurements have been performed on a purple membrane sheet deposited on a mica surface. Figure 4 shows the topography and the phase image of a PM sheet deposited on mica. The phase image (Figure 4b) shows a distinctive contrast difference among the mica, the extracellular (EC) and the cytoplasmic (CP) protein membrane (bacteriorhodopsin, bR) surfaces. The CP region has an average thickness of 4.4 nm, while EC patches had a thickness of 4.9 nm. The phase image also enables the viewer to distinguish two regions of the extracellular surface with different orientations (Figure 4c). A zoom in a region of the EC side shows that molecular resolution is also achieved (Figures 4d,e). The characteristic trimer of the bR molecule in the extracellular interface is resolved in

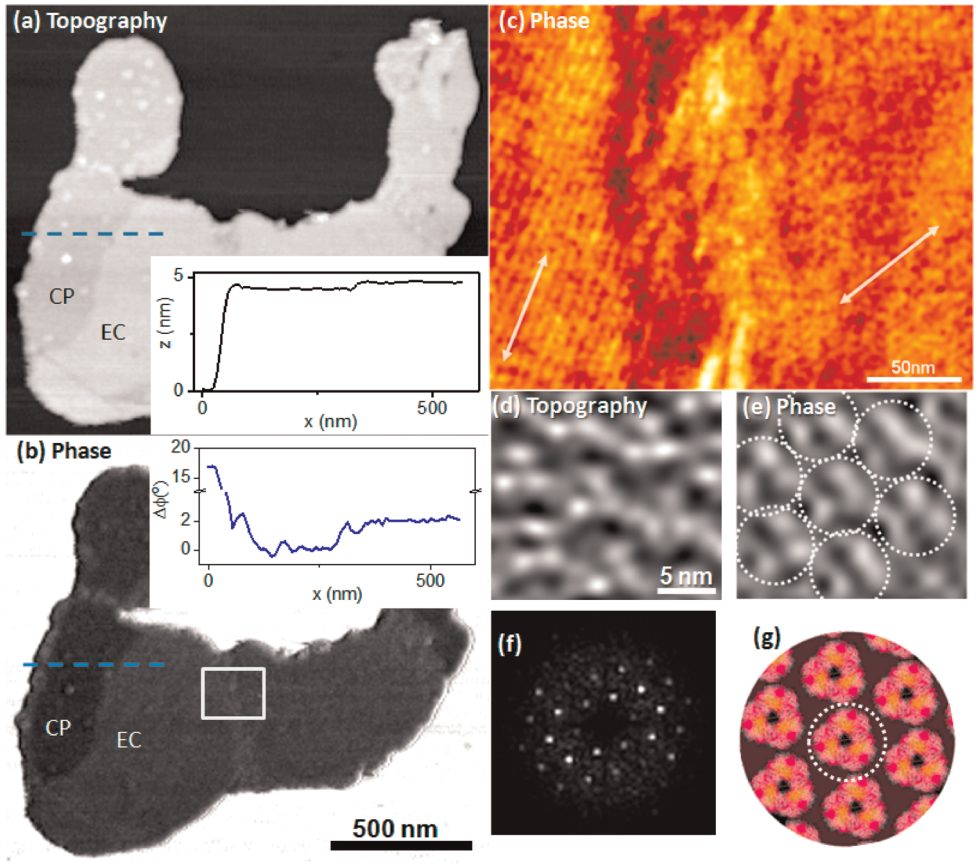

Figure 4. Topography and phase-shift image of a purple membrane sheet on mica. Imaged taken in a buffer solution (10 mM Tris, 150 mM KCl, pH 8.1). (a) Topography. The cross-section along the dashed line shows the thickness of the PM. (b) Phase-shift image. Two different phase-shift values are observed on the membrane patch. Those values are related to the presence of ordered arrays of bR in EC and CP sides. The cross-section along the dashed line shows the phase-shift difference between the mica and the different PM sides. (c) High resolution phase image of a region that shows the interface between two different orientation of the protein lattice (marked by in square in panel b) ($A_{sp} = 0.6A_0$, $A_0 = 8$ nm)). (d) Molecular resolution image with the characteristic trimer of the extracellular interface (topography). (e) Molecular resolution phase image. The diameter of the circles is 6.6 nm which agrees with the bR nominal size. (f) Two-dimensional power spectrum of the image shown in panel e. (g) bR organization in PM. The bR structure is the 1AT9 from the protein data bank. The circle encloses a single bR protein.

the phase image (Figure 4e). The two-dimensional power spectrum obtained from Figure 4e is shown in Figure 4f. A scheme of the two-dimensional structure of the PM is shown in Figure 4g.

On the basis of the simulations like the ones shown in Figure 2, we propose that the phase contrast observed in Figure 4b arises in part from the differences in the elastic properties that exist among the mica and the protein loops in the EC ($E \approx 50$ MPa) and the CP ($E \approx 10$ MPa) sides.[45] This is confirmed by recording the Fourier transform of the measured tip motion on mica, EC, and CP sides (Figure 5a). The HD decreases by moving from the mica to the EC and from there to the CP side (Figure 5b). The amplitude of the harmonics is larger in mica because the elastic modulus of mica is higher than in either EC or CP. Similarly, the higher harmonics in the EC side are higher than in the CP side. Those findings are consistent with the stiffness measurements obtained by using torsional harmonic AFM.[45]

The above results show that the theory describes at least qualitatively the experimental findings. We remark that the contrast observed between the mica and the bR patches coincides with the one reported by Melcher *et al.*[37] This underlines the reproducibility of the compositional contrast provided by phase images. At the molecular resolution level Figure 4e shows that the bR region has a higher phase shift than the lipid region. It is tempting to attribute the contrast to the differences in the elastic properties between the bR and the lipids. This would be in agreement with the findings provided by force spectroscopy curves that show the bR with higher stiffness than the lipid region;[46] however, the observed contrast could also reflect the existence of topographic changes when the tip is on top of the protein loops with respect to the situation when the tip is bridging two bRs.[47]

We have performed two types of comparisons to validate quantitatively the theory. Already mentioned was the agreement that exists between the theoretical

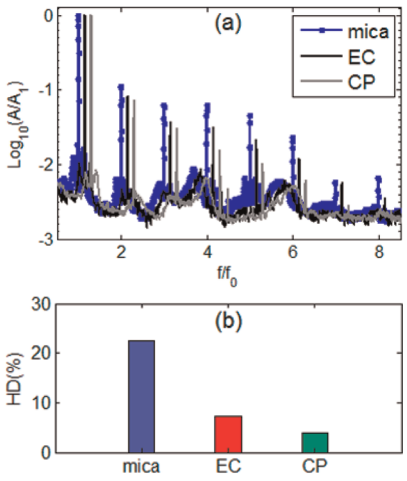

Figure 5. (a). Experimental Fourier transform of the tip motion measured on mica, EC, and CP regions. For clarity, the curves are shifted in the frequency axis. (b) Harmonic distortion for mica, EC, and CP regions derived from panel a.

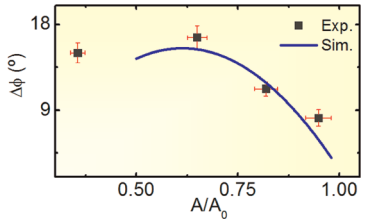

Figure 6. Comparison between the measured and the calculated phase-shift difference curves for a PM deposited (CP regions) on a mica surface (A_0 = 9.4 nm). The simulations have been performed for PM and mica characterized, respectively, by E = 50 MPa, η = 10 Pa s and E = 10 GPa.

results derived from eq 8 and the full numerical solution of the modified Euler–Bernoulli Equation (Figure 1b). However, we consider more illustrative the comparison between the theory and the experimental data obtained on a PM deposited on mica (Figure 6). The experimental points follow the trend described by the theoretical curve. They also show a good quantitative agreement (the relative error is below 10%). The data also show that the relative phase-shift difference $\Delta\phi = \phi_{mica} - \phi_{PM}$ in the $A_{sp} \in [1-0.5]$ range increases by lowering the free amplitude (not shown). We remark that for small A_{sp} values, say below 0.5, the model used to simulate the mechanical properties of PM on mica fails because the membrane deformation (3–4 nm) becomes comparable to the membrane thickness (~5 nm). Additionally, the present model for the PM–mica interface does not consider the mechanical coupling between the PM and the mica.

At the nanoscale, the repulsive region of the conservative force can be related to the elastic modulus.[48] At the molecular scale such as the one shown in Figure 4c, the phase contrast can be related to variations in the flexibility of the molecules.[45] At the atomic level, it has been shown that the conservative region of the force is a signature of the chemical species in the surface.[49] Different factors might contribute to dissipation. At the meso and nano scales viscosity, adhesion, and friction are relevant factors. Down to the molecular level and, for experiments that do not involve breaking or forming chemical bonds,[50] it has been shown that dissipation is a signature of the presence of atomic and molecular reorganization processes.[23]

CONCLUSION

We provide a theoretical model that explains the origin of the phase contrast observed in amplitude modulation AFM. The theory applies for experiments performed in liquid and air. Molecular resolution experiments performed on a purple membrane surface deposited on a mica surface confirm the theory. The phase shift has two contributions, one is derived from the conservative part of the tip–surface interaction force, and thus from the elastic properties of the sample. The other contribution arises from the energy dissipated by the nonconservative interactions. In a given experiment, the properties of the sample, namely its compliance and the dissipation mechanisms are the factors that control the phase shift. In particular, the phase contrast while imaging soft and viscous materials is dominated by dissipation. On the other hand, the phase contrast while imaging stiff and elastic materials is related to the presence of higher harmonics in the tip's oscillation. Those harmonics are generated by the nonlinear tip–surface forces. On heterogeneous materials a comparison of the higher harmonics components could be used to determine whether the observed contrast comes from changes in the local elastic properties or from differences in inelastic interactions.

METHODS

Purple membrane (PM) is a model surface in AFM because it has a well-defined morphology, and the protein periodicity is a test for the lateral resolution of any AFM methodology in liquid.[44] A drop of 100 μg/ml of purple membrane in buffer (10 mM Tris, 150 mM KCl, pH 8.1) was deposited onto freshly cleaved mica for 30 minutes, and gently washed with the same buffer to remove weakly attached patches. The images were taken in the same buffer. The experiments have been performed in liquid (10 mM Tris, 150 mM KCl, pH 8.1) by using triangular cantilevers (OTR4 Bruker) with k_1 = 0.1 N m^{-1}, f_1 = 8.4 kHz, Q_1 = 2.1, k_2 = 4.4 N m^{-1}, f_2 = 65 kHz, Q_2 = 3 and (MAC lever VI) with k_1 = 0.18 N m^{-1}, f_1 = 18.6 kHz, Q_1 = 1.7, k_2 = 8.18 N m^{-1}, f_2 = 172 kHz, Q_2 = 4.

Conflict of Interest: The authors declare no competing financial interest.

Acknowledgment. We thank Elena T. Herruzo, Javier Tamayo, and Kislon Voitchovsky for their comments and suggestions.

This work was supported by the Spanish Ministry of Science (MICINN) through Grants CSD2010-00024 and MAT2009-08650. J.R.R. has a JAE-Predoc fellowship from the European Social fund.

REFERENCES AND NOTES

1. Garcia, R.; Magerle, R.; Perez, R. Nanoscale Compositional Mapping with Gentle Forces. *Nat. Mater.* **2007**, *6*, 405–411.
2. Magonov, S. N.; Elings, V.; Papkov, V. S. AFM Study of Thermotropic Structural Transitions in Poly(diethylsiloxane). *Polymer* **1997**, *38*, 297–307.
3. Suo, Z.; Yang, X.; Avci, R.; Kellerman, L.; Pascual, D. W.; Fries, M.; Steele, A. HEPES-Stabilized Encapsulation of Salmonella Typhimutium. *Langmuir* **2007**, *23*, 1365–1374.
4. Schweitzer, M. H.; Suo, Z.; Avci, R.; Asara, J. M.; Allen, M. A.; Arce, F. T.; Horner, J. R. Analyses of Soft Tissue from Tyrannosaurus Rex Suggest the Presence of Protein. *Science* **2007**, *316*, 277–280.
5. Hobbs, J. K.; Farrance, O. E.; Kailas, L. How Atomic Force Microscopy Has Contributed to Our Understanding of Polymer Crystallization. *Polymer* **2009**, *50*, 4281–4292.
6. Voitchovsky, K.; Kuna, J. J.; Contera, S. A.; Tosatti, E.; Stellacci, F. Direct Mapping of the Solid−Liquid Adhesion with Subnanometer Resolution. *Nat. Nanotechnol.* **2010**, *5*, 401–405.
7. Tetard, L.; Passian, A.; Thundat, T. New Modes for Subsurface Atomic Force Microscopy through Nanomechanical Coupling. *Nat. Nanotechnol.* **2010**, *5*, 105–109.
8. Zhao, Y.; Cheng, Q.; Qian, M.; Cantrell, J. H. Phase Image Contrast Mechanism in Intermittent Contact Atomic Force Microscopy. *J. Appl. Phys.* **2010**, *108*, 094311.
9. Nightingale, L. M.; Lee, S.-Y.; Engeseth, N. J. Impact of Storage on Dark Chocolate: Texture and Polymorphic Changes. *J. Food Sci.* **2011**, *76*, C142–C153.
10. Nie, N. Y.; Taylor, A. R.; Lau, W. M.; MacFabe, D. F. Subcellular Features Revealed on Fixed Rat Brain Sections by Phase Imaging. *Analyst* **2011**, *136*, 2270–2276.
11. Liu, Y. H.; Wang, D.; Nakajima, K.; Zhang, W.; Hirata, A.; Nishi, T.; Inoue, A.; Chen, M. W. Characterization of Nanoscale Mechanical Heterogeneity in a Metallic Glass by Dynamic Force Microscopy. *Phys. Rev. Lett.* **2011**, *106*, 125504.
12. Spitzner, E. C.; Riesch, C.; Magerle, R. Subsurface Imaging of Soft Polymeric Materials with Nanoscale Resolution. *ACS Nano* **2011**, *5*, 315–320.
13. O'Dea, J. R.; Buratto, S. K. Phase Imaging of Proton Exchange Membranes under Attractive and Repulsive Tip−Sample Interaction Forces. *J. Phys. Chem. B* **2011**, *115*, 1014–1020.
14. Tamayo, J.; Garcia, R. Relationship between Phase Shift and Energy Dissipation in Tapping-Mode Scanning Force Microscopy. *Appl. Phys. Lett.* **1998**, *73*, 2926–2928.
15. Cleveland, J. P.; Anczykowski, B.; Schmid, A. E.; Elings, V. B. Energy Dissipation in Tapping-Mode Atomic Force Microscopy. *Appl. Phys. Lett.* **1998**, *72*, 2613–2615.
16. Martin, P.; Marsaudon, S.; Aime, J. P.; Benneteau, B. Experimental Determination of Conservative and Dissipative Parts in the Tapping Mode of a Grafted Layer: Comparison with Frequency Modulation Data. *Nanotechnology* **2005**, *16*, 901–907.
17. Proksch, R.; Kalinin, S. V. Energy Dissipation Measurements in Frequency Modulated Scanning Probe Microscopy. *Nanotechnology* **2010**, *21*, 455705.
18. Proksch, R.; Yablon, D. G. Loss Tangent Imaging: Theory and Simulations of Repulsive-Mode Tapping Atomic Force Microscopy. *Appl. Phys. Lett.* **2012**, *100*, 073106.
19. Santos, S.; Thomson, N. H. Energy Dissipation in a Dynamic Nanoscale Contact. *Appl. Phys. Lett.* **2011**, *98*, 013101.
20. Santos, S.; Barcons, V.; Verdaguer, A.; Font, J.; Thomson, N. H.; Chiesa, M. How Localized are Energy Dissipation Processes in Nanoscale Interactions? *Nanotechnology* **2011**, *22*, 345401.
21. Garcia, R.; Gomez, C. J.; Martinez, N. F.; Patil, S.; Dietz, C.; Magerle, R. Identification of Nanoscale Dissipation Processes by Dynamic Atomic Force Microscopy. *Phys. Rev. Lett.* **2006**, *97*, 016103.
22. Martinez, N. F.; Garcia, R. Measuring Phase Shifts and Energy Dissipation with Amplitude Modulation Atomic Force Microscopy. *Nanotechnology* **2006**, *17*, S167–S172.
23. Martinez, N. F.; Kaminski, W.; Gomez, C. J.; Albonetti, C.; Biscarini, F.; Perez, R.; Garcia, R. Molecular Scale Energy Dissipation in Oligothiophene Monolayers Measured by Dynamic Force Microscopy. *Nanotechnology* **2009**, *20*, 434021.
24. Gomez, C. J.; Garcia, R. Determination and Simulation of Nanoscale Energy Dissipation Processes in Amplitude Modulation AFM. *Ultramicroscopy* **2010**, *110*, 626–633.
25. Shekhawat, G. S.; Dravid, V. P. Nanoscale Imaging of Buried Structures *via* Scanning Near-Field Ultrasound Holography. *Science* **2005**, *310*, 89–92.
26. Zerson, M.; Spitzner, E. C.; Riesch, C.; Lohwasser, R.; Thelakkat, M.; Magerle, R. Subsurface Mapping of Amorphous Surface Layers on Poly(3-hexylthiophene). *Macromolecules* **2011**, *44*, 5874–5877.
27. Kuna, J. J.; Voïtchovsky, K.; Singh, C.; Jiang, H.; Mwenifumbo, S.; Ghorai, P. K.; Stevens, M. M.; Glotzer, S. C.; Stellacci, F. The Effect of Nanometer-Scale Structure on Interfacial Energy. *Nat. Mater.* **2009**, *8*, 837–842.
28. Martinez, N. F.; Patil, S; Lozano, J. R.; Garcia, R. Enhanced Compositional Sensitivity in Atomic Force Microscopy by the Excitation of the First Two Flexural Modes. *Appl. Phys. Lett.* **2006**, *89*, 153115.
29. Dietz, C.; Zerson, M.; Riesch, C.; Gigler, A. M.; Stark, R. W.; Rehse, N.; Magerle, R. Nanotomography with Enhanced Resolution Using Bimodal AFM. *Appl. Phys. Lett.* **2008**, *92*, 143107.
30. Albonetti, C.; Casalini, S.; Borgatti, F.; Floreano, F; Biscarini, F. Morphological and Mechanical Properties of Alkanethiol Self-Assembled Monolayers Investigated *via* Bimodal AFM. *Chem. Commun. (Cambridge, U. K.)* **2011**, *47*, 8823–8825.
31. Li, J. W.; Cleveland, J. P.; Proksch, R. Bimodal Magnetic Force Microscopy: Separation of Short and Long Range Forces. *Appl. Phys. Lett.* **2009**, *94*, 163118–3.
32. Dietz, C.; Herruzo, E. T.; Lozano, J. R.; Garcia, R. Nanomechanical Coupling Enables Detection and Imaging of 5 nm Superparamagnetic Particles in Liquid. *Nanotechnology* **2011**, *22*, 125708.
33. San Paulo, A.; Garcia, R. Tip-Surface Forces, Amplitude, and Energy Dissipation in Amplitude Modulation (Tapping-Mode) Force Microscopy. *Phys. Rev. B* **2001**, *64*, 193411.
34. Bar, G.; Delineau, L.; Brandsch, R.; Bruch, M.; Whangbo, M. H. Importance of the Indentation Depth in Tapping-Mode AFM Study of Compliant Materials. *Appl. Phys. Lett.* **1999**, *75*, 4198–4200.
35. Bodiguel, H.; Montes, H.; Fretigny, C. Depth Sensing and Dissipation in Tapping Mode Atomic Force Microscopy. *Rev. Sci. Instrum.* **2004**, *75*, 2529–2535.
36. Tamayo, J. Energy Dissipation in Tapping-Mode Scanning Force Microscopy with Low Quality Factors. *Appl. Phys. Lett.* **1999**, *75*, 3569–3571.
37. Melcher, J.; Xu, X.; Raman, A.; Carrasco-Pulido, C.; Gomez-Herrero, J.; de Pablo, P. J.; Carrascosa, J. L. Origins of Phase Contrast in the Atomic Force Microscope in Liquids. *Proc. Natl. Acad. Sci. U.S.A.* **2009**, *106*, 13655–13660.
38. Xu, X.; Melcher, J.; Basak, S.; Reinferberger, R.; Raman, A. Compositional Contrast of Biological Materials in Liquid Using the Momentary Excitation of Higher Eigenmodes in Dynamic Atomic Force Microscopy. *Phys. Rev. Lett.* **2009**, *102*, 060801.
39. Xu, X.; Melcher, J.; Raman, A. Accurate Force Spectroscopy in Tapping Mode Atomic Force Microscopy in Liquids. *Phys. Rev. B* **2010**, *81*, 035407.
40. Basak, S.; Raman, A. Dynamics of Tapping Mode Atomic Force Microscopy in Liquids: Theory and Experiments. *Appl. Phys. Lett.* **2007**, *91*, 064107.
41. Stark, M.; Stark, R. W.; Heckl, W. H.; Guckenberger, R. Inverting Dynamic Force Microscopy: From Signals to Time-Resolved Interaction Forces. *Proc. Natl. Acad. Sci. U.S.A.* **2002**, *99*, 8473–8478.

42. Sahin, O.; Quate, C. F.; Solgaard, O.; Atalar, A. An Atomic Force Microscope Tip Designed to Measure Time-Varying Nanomechanical Forces. *Nat. Nanotechnol.* **2007**, *2*, 507–514.
43. Derjaguin, B. V.; Muller, V. M.; Toporov, Y. P. Effect of Contact Deformations on Adhesion of Particles. *J. Colloid Interface Sci.* **1975**, *53*, 314–326.
44. Muller, D. J.; Engel., A. Atomic Force Microscopy and Spectroscopy of Native Membrane Proteins. *Nat. Protocols* **2007**, *2*, 2191–2197.
45. Dong, M.; Husale, S.; Sahin, O. Determination of Protein Structural Flexibility by Microsecond Force Spectroscopy. *Nat. Nanotechnol.* **2009**, *4*, 514–517.
46. Rico, F.; Su, C.; Scheuring, S. Mechanical Mapping of Single Membrane Proteins at Submolecular Resolution. *Nano Lett.* **2011**, *11*, 3983–3986.
47. Stark, M.; Möller, C.; Müller, D. J.; Guckenberger, R. From Images to Interactions: High-Resolution Phase Imaging in Tapping-Mode Atomic Force Microscopy. *Biophys. J.* **2001**, *80*, 3009–3018.
48. Luan, B.; Robbins, M. O. The Breakdown of Continuum Models for Mechanical Contacts. *Nature* **2005**, *435*, 929–932.
49. Sugimoto, Y.; Pou, P.; Abe, M.; Jalinek, P.; Perez, R.; Morita, S.; Custance, O. Chemical Identification of Individual Surface Atoms by Atomic Force Microscopy. *Nature* **2007**, *446*, 64–67.
50. Kawai, S.; Canova, F. F.; Glatzel, T.; Adam S. Foster, A. S.; Meyer, E. Atomic-Scale Dissipation Processes in Dynamic Force Spectroscopy. *Phys. Rev. B* **2011**, *84*, 115415.